nature genetics

Blindness and auditory impairment caused by loss of the sodium bicarbonate cotransporter NBC3

Dean Bok[1], Gary Galbraith[2], Ivan Lopez[3], Michael Woodruff[4], Steven Nusinowitz[5], Hector BeltrandelRio[6], Wenhu Huang[6], Shulei Zhao[6], Robert Geske[6], Charles Montgomery[6], Isaac Van Sligtenhorst[6], Carl Friddle[6], Kenneth Platt[6], Mary Jean Sparks[6], Alexander Pushkin[7], Natalia Abuladze[7], Akira Ishiyama[3], Ramanath Dukkipati[7], Weixin Liu[7] & Ira Kurtz[7]

Normal sensory transduction requires the efficient disposal of acid (H^+) generated by neuronal and sensory receptor activity[1,2]. Multiple highly sensitive transport mechanisms have evolved in prokaryotic and eukaryotic organisms to maintain acidity within strict limits[3–5]. It is currently assumed that the multiplicity of these processes provides a biological robustness[6]. Here we report that the visual and auditory systems have a specific requirement for H^+ disposal mediated by the sodium bicarbonate cotransporter NBC3 (refs. 7,8). Mice lacking NBC3 develop blindness and auditory impairment because of degeneration of sensory receptors in the eye and inner ear as in Usher syndrome[9]. Our results indicate that in certain sensory organs, in which the requirement to transduce specific environmental signals with speed, sensitivity and reliability is paramount, the choice of the H^+ disposal mechanism used is limited.

The strategy used to generate and identify mice with targeted disruption in NBC3 (encoded by *Slc4a7*) is shown in **Figure 1**. *Slc4a7*$^{-/-}$ mice grew and developed normally, appeared grossly normal, were fertile and had no anatomic, behavioral, serum or urine electrolyte abnormalities. Fundus examination at one month was normal. By four months of age, however, the fundi of *Slc4a7*$^{-/-}$ mice were markedly abnormal (**Fig. 2a**,**b**). The retinas of *Slc4a7*$^{-/-}$ mice also appeared morphologically normal at one month of age in comparison with those of *Slc4a7*$^{+/+}$ and *Slc4a7*$^{+/-}$ mice (**Fig. 2c–e**). By two months of age, the inner retina of *Slc4a7*$^{-/-}$ mice retained a normal phenotype but clear differences were apparent in the photoreceptor region (**Fig. 2f–i**). Outer segments were shorter and the number of photoreceptor cell nuclei in the outer nuclear layer (ONL) was lower, reducing the ONL thickness to ~75% of normal, suggesting a substantial amount of cell death. By six months of age, the photoreceptor cells had degenerated considerably in retinas of *Slc4a7*$^{-/-}$ mice. The ONL in the superior

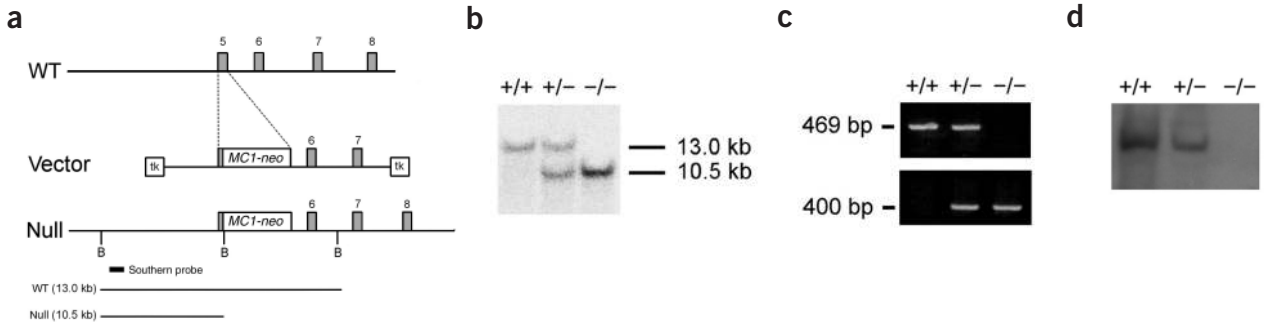

Figure 1 Targeted disruption of *Slc4a7*. (**a**) Structural arrangement of 129 Sv/Ev^{brd} mouse gene *Slc4a7*. Restriction map of wild-type mouse *Slc4a7*, the *Slc4a7* targeting vector and a diagram of the mutated *Slc4a7* allele after homologous recombination are shown. B, *Bam*H1. (**b**) Southern-blot hybridization. Disruption of mouse *Slc4a7* by homologous recombination produced a 10.5-kb band using *Bam*H1 digested genomic DNA. (**c**) PCR genotyping of mutant mice. (**d**) Western-blot analysis of protein samples prepared from eyes of wild-type (*Slc4a7*$^{+/+}$; +/+), heterozygous (*Slc4a7*$^{+/-}$; +/–) and null (*Slc4a7*$^{-/-}$; –/–) mice using the C-terminal antibody to NBC3 (refs. 29,30).

[1]Department of Neurobiology, Jules Stein Eye Institute and Brain Research Institute; [2]Department of Psychiatry and Biobehavioral Sciences; [3]Department of Head and Neck Surgery; [4]Department of Physiological Sciences; and [5]Department of Ophthalmology, Jules Stein Eye Institute; David Geffen School of Medicine at UCLA, Los Angeles, California, 90095, USA. [6]Lexicon Genetics, The Woodlands, Texas 77381, USA. [7]Division of Nephrology, Department of Medicine, David Geffen School of Medicine at UCLA, Room 7-155 Factor Building, 10833 Le Conte Avenue, Los Angeles, California, 90095, USA. Correspondence should be addressed to I.K. (Ikurtz@mednet.ucla.edu).

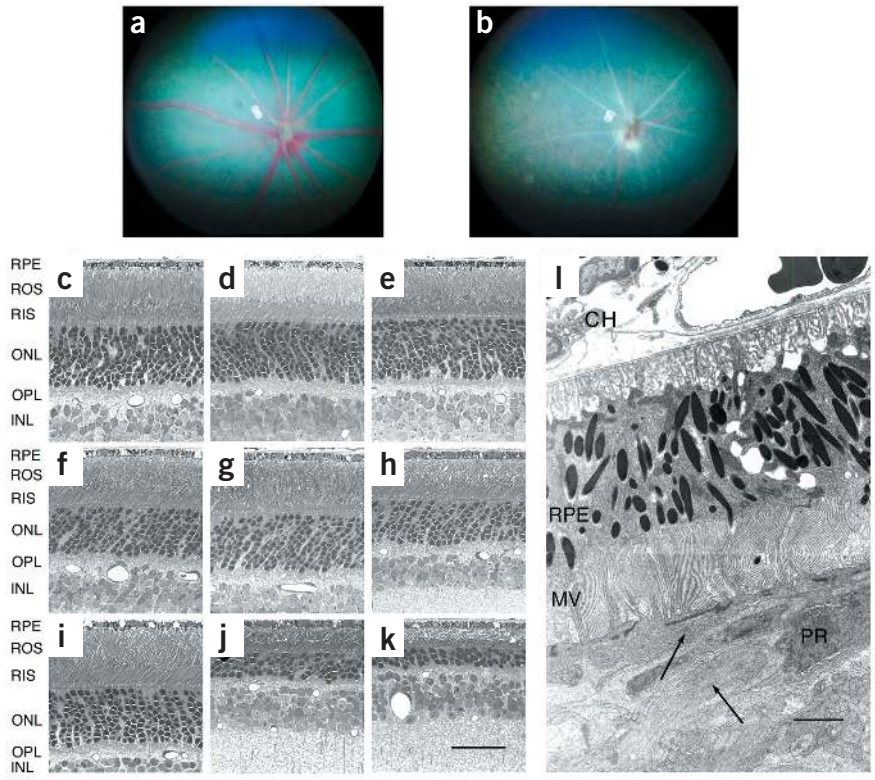

Figure 2 Funduscopic and histologic changes of the retina. (**a**) Normal fundus of a *Slc4a7*$^{+/+}$ four-month-old mouse. (**b**) Fundus of a four-month-old *Slc4a7*$^{-/-}$ littermate showing marked blood vessel attenuation and diffuse granularity as typically observed in retinitis pigmentosa. (**c–k**) Retinas of *Slc4a7*$^{+/+}$, *Slc4a7*$^{+/-}$ and *Slc4a7*$^{-/-}$ mice of various ages. The layers shown include the retinal pigment epithelium (RPE), outer segment (ROS), inner segment (RIS), outer nuclear layer (ONL), outer plexiform layer (OPL) and inner nuclear layer (INL). Scale bar = 50 μm. At one month of age, *Slc4a7*$^{-/-}$ mice (**e**) had normal retinas in terms of ONL thickness and length of the outer and inner segment compared with *Slc4a7*$^{+/+}$ (**c**) and *Slc4a7*$^{+/-}$ mice (**d**). By two months of age, *Slc4a7*$^{+/+}$ (**f**) and *Slc4a7*$^{+/-}$ mice (**g**) remained indistinguishable, but *Slc4a7*$^{-/-}$ mice (**h**) had substantial retinal changes. The outer segments were shorter and the outer nuclear layer had become thinner by approximately one layer of nuclei. At eight months of age, the retinas of *Slc4a7*$^{+/-}$ mice (**i**) were unchanged; retinas were unchanged in *Slc4a7*$^{+/-}$ and *Slc4a7*$^{+/+}$ mice up to 14 months of age (data not shown). Retinas of six-month-old *Slc4a7*$^{-/-}$ mice, however, had lost ~60% of ONL thickness in the inferior hemisphere (**j**) and ~75% of its thickness in the superior hemisphere (**k**). (**l**) Electron micrograph montage of a retina from an 11-month-old *Slc4a7*$^{-/-}$ mouse. The image was taken from the superior hemisphere in which nearly all of the photoreceptor (PR) cells had died. The highly infolded basal surface of the retinal pigment epithelium (RPE) was normal and was in contact with the choroidal layer (CH). The RPE structure appeared normal, as did the vasculature of the choroid. In the absence of photoreceptor outer segments, nerve cell processes of inner retinal neurons (arrows) abutted the tips of the RPE microvilli (MV). Scale bar = 7 μm.

retina was reduced to ~25% of normal thickness (**Fig. 2j**) and the ONL in the inferior retina was reduced to ~40% of normal thickness (**Fig. 2k**). By 14 months of age (data not shown), the superior retina had lost virtually all photoreceptors and only a few scattered nuclei remained, whereas the inferior retina retained about 35% of original thickness. For all genotypes and ages, the layers of the retina proximal to the photoreceptor cells appeared normal. Electron microscopy of the superior retina at 11 months of age showed that it was nearly devoid of photoreceptor cells (**Fig. 2l**). In the absence of photoreceptor outer segments, retinal pigment epithelium (RPE) microvilli filled the void and nerve cell processes of inner retinal neurons abutted the tips of the RPE microvilli.

Selective loss of photoreceptor cells is a feature of several retinopathies, although the rate of degeneration can vary considerably. A null mutation in the beta subunit of cGMP phosphodiesterase in the *Pde6b*$^{rd1/rd1}$ (also called *rd*$^{-/-}$) mouse that increases rod photoreceptor cGMP causes all of the rod photoreceptors to die by post partum d 20 (ref. 10). Conversely, a null mutation in *Rds* that results in no Rds/peripherin synthesis causes slow photoreceptor death that requires about one year for completion[11]. The retina of the *Slc4a7*$^{-/-}$ mouse resembles the latter model in terms of rate of progression.

Rod-mediated electroretinograms (ERGs) are shown in **Figure 3a**. The parameters V_{max}, the maximum saturated b-wave amplitude, and *k*, the semi-saturation intensity, are depicted at all ages tested in **Figure 3b**. There was a loss of V_{max} amplitude and an elevation of *k* with age in *Slc4a7*$^{-/-}$ mice. By one year of age, V_{max} was less than 10% of the corresponding value at one month, and *k* had shifted upwards by approximately 0.4 log units, more than doubling the semi-saturation intensity. An analysis of the photocurrents of rods of *Slc4a7*$^{-/-}$ mice (**Fig. 3c–f**) indicates that the propensity for photoreceptor degeneration in these mice is not accompanied by substantial changes in the sensitivity of surviving rods. The rods from 2.5-month-old *Slc4a7*$^{+/+}$ mice and surviving rods from retinas of age-matched *Slc4a7*$^{-/-}$ mice were exposed to various intensities of 500-nm light to determine the sensitivity of the rods for photocurrent generation. The kinetics, amplitudes and sensitivities of the responses from just above threshold to near saturation were similar (**Fig. 3c**,**d**). The average relative responses versus flash intensity were similar in *Slc4a7*$^{-/-}$ mice and *Slc4a7*$^{+/+}$ mice (**Fig. 3e**). Half-maximal saturation was 3.2×10^2 and 3.4×10^2 photons μm^{-2}, respectively. The amplitude of the single-photon responses for *Slc4a7*$^{-/-}$ mice was 0.78 ± 0.09 pA ($n = 12$) and for *Slc4a7*$^{+/+}$ mice was 0.77 ± 0.11 pA ($n = 16$; **Fig. 3f**). The latencies and time to peaks of the single-photon responses were also similar: 58 ± 6 ms and 213 ± 16 ms, respectively, in *Slc4a7*$^{-/-}$ mice ($n = 12$) and 72 ± 6 ms and 216 ± 24 ms, respectively, in *Slc4a7*$^{+/+}$ mice ($n = 16$).

Confocal immunofluorescence images of retinas of *Slc4a7*$^{+/+}$ mice showed that the transporter was expressed in the outer plexiform layer, where it was detected in the photoreceptor synaptic terminals (**Fig. 4a**,**c**). In retinas from *Slc4a7*$^{-/-}$ mice, NBC3 was not expressed (**Fig. 4b**). In addition, apoptotic nuclei were detected in photoreceptors from *Slc4a7*$^{-/-}$ mice (**Fig. 4e**) but not in retinas of control mice (**Fig. 4d**).

Slc4a7$^{-/-}$ mice provide the first example of photoreceptor degeneration resulting from loss of function of an acid-disposal transporter. Although retinal degeneration resulting from genetic defects is usually characterized by apoptosis in photoreceptor cells[12], it was not

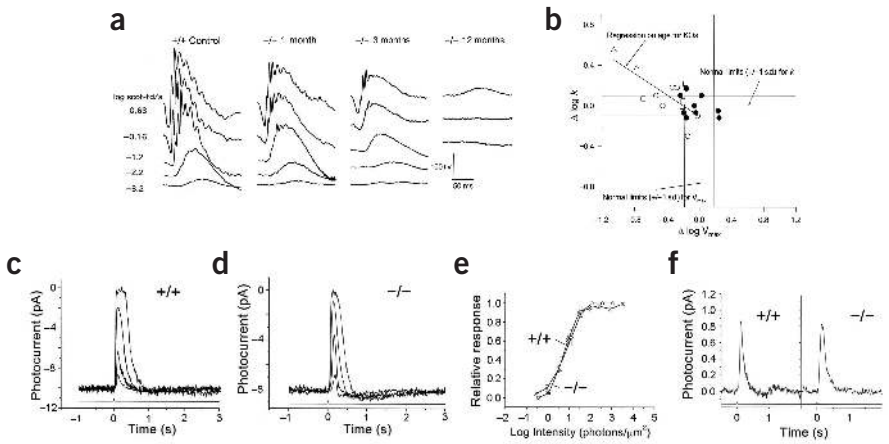

Figure 3 ERGs and single-rod photocurrent responses in *Slc4a7*$^{-/-}$ mice. (**a**) Rod-mediated ERGs for selected intensities from a representative *Slc4a7*$^{+/+}$ mouse and from *Slc4a7*$^{-/-}$ mice at 1, 3 and 12 months of age. Stimulus intensities are shown on the vertical scale. Calibration bars are shown in the inset on the right. (**b**) Quantitative ERG results in *Slc4a7*$^{-/-}$ mice. The parameters log *k* and log V_{max} were derived from the fit of the Naka-Ruston equation across all ages tested. Log *k* and log V_{max} are expressed as the differences from age-matched control mice (closed circles). A value of 0.0 for each parameter corresponds to the mean for that parameter obtained from the *Slc4a7*$^{+/+}$ mice. Open circles, squares and triangles show individual data for 1-, 2- and 12-month-old *Slc4a7*$^{-/-}$ mice, respectively. The vertical and horizontal lines show ± 1 s.d. for the parameters V_{max} and *k*, respectively. (**c–f**) Single-rod photocurrent responses in 2.5-month-old mice. Suction electrode photoresponse currents are shown for (**c**) *Slc4a7*$^{+/+}$ and (**d**) *Slc4a7*$^{-/-}$ mice at four light intensities: 55, 200, 630 and 1,900 photons per μm^2 per s. Each response is the average current from 10–20 20-ms flashes of 500-nm light. (**e**) The relative responses of rods from threshold to response saturation at various flash strengths. The results depict the mean ± s.e.m. of rods from *Slc4a7*$^{+/+}$ and *Slc4a7*$^{-/-}$ mice (multiple responses were averaged relative to the maximum response). (**f**) Single-photon responses for rods from *Slc4a7*$^{+/+}$ and *Slc4a7*$^{-/-}$ mice.

previously known that the molecular events involving the apoptotic cascade could be initiated as a result of loss of sodium bicarbonate cotransport function. The maintenance of normal ion homeostasis is clearly important in preventing retinal degeneration, as suggested by the role for intracellular Ca^{2+} in mediating photoreceptor death in genetic and environment-associated retinopathies[13]. Dynamic changes in outer segment Ca^{2+} levels control sensitivity to light in rods and have been linked to rod pathology, but the finding that rod sensitivity to light is unaffected in surviving photoreceptors in *Slc4a7*$^{-/-}$ mice (**Fig. 3b–e**) suggests that Ca^{2+} homeostasis in the outer segment is normal[13,14]. In the mammalian photoreceptors where NBC3 is localized (**Fig. 4a**,**c**), however, Ca^{2+} transporters whose function is regulated by changes in pH and that may have a role in the downstream events leading to apoptotic cell death in *Slc4a7*$^{-/-}$ mice are expressed in the synaptic terminals. Specifically, in photoreceptor synaptic terminals, the plasma membrane calcium ATPase (PMCA1 and PMCA4 isoforms) can extrude Ca^{2+} in exchange for H^+ (refs. 13,15,16). NBC3-mediated bicarbonate flux in the synaptic terminal could therefore be essential in buffering this H^+ load and thereby maintaining a normal rate of PMCA-mediated Ca^{2+} efflux (**Fig. 4f**). Moreover, it has previously been hypothesized that PMCA in the synaptic terminals of mammalian photoreceptors may complex with PSD-95, a membrane-associated guanyl kinase protein known to organize neurotransmitter receptors and ion channels[13,17]. Both PMCAs and NBC3 have C-terminal PDZ-interacting motifs and could therefore potentially complex through the PDZ domain–containing protein PSD-95 to enhance the efficiency of H^+ buffering in the synaptic terminal[18,19]. In addition to PMCA, previous studies have shown that the function of L-type voltage-gated Ca^{2+} channels in the photoreceptor synaptic terminus is exquisitely sensitive to changes in pH[20,21]. Therefore, presynaptic Ca^{2+} currents are dependent on the efficient buffering of H^+ loads in the photoreceptor synaptic terminus where NBC3 is located.

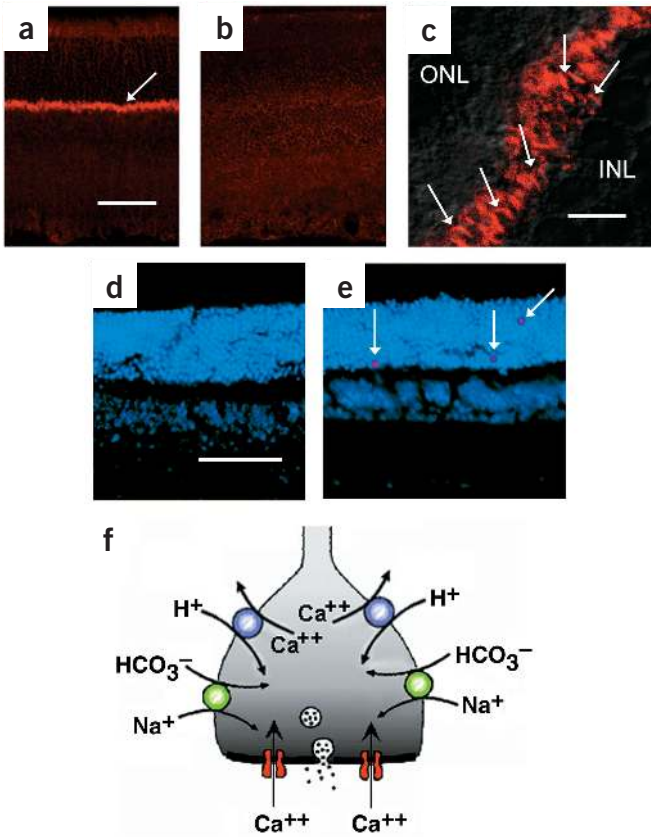

Figure 4 Localization of NBC3 in the mouse retina and apoptosis of photoreceptors in *Slc4a7*$^{-/-}$ mice. (**a**) Confocal fluorescence images of retina from three-month-old *Slc4a7*$^{+/+}$ mice showing staining of the outer plexiform layer (arrow). An identical pattern of expression was detected at ages 1–12 months. Scale bar = 50 μm. (**b**) Absence of staining in the retina of *Slc4a7*$^{-/-}$ mice. (**c**) Higher magnification of the outer plexiform layer showing localization of NBC3 in the synaptic termini of photoreceptors (arrows). ONL, outer nuclear layer; INL, inner nuclear layer. Scale bar = 8 μm. (**d**) Absence of apoptotic nuclei in retinas of 2.5-month-old *Slc4a7*$^{+/+}$ mice. Nuclei (blue) are stained with Hoechst dye. (**e**) Apoptotic nuclei are shown (red, arrows) in retinas of 2.5-month-old *Slc4a7*$^{-/-}$ mice. Scale bar = 100 μm. (**f**) Model for photoreceptor synaptic terminal ion flux.

Slc4a7$^{-/-}$ mice (ages 1–12 months) had no apparent abnormalities in vestibular and motor function during rotarod and tilt-table experiments, but they did have auditory impairment. Auditory brainstem responses (ABR) were recorded from mice at one and three months of age. The *Slc4a7*$^{-/-}$ mice had markedly lower ABR amplitudes by three months of age (**Fig. 5a**,**b**). ABR waveforms and mean ABR thresholds in response to tone bursts are depicted in **Figure 5c**,**d**. Above 2 kHz, ABR thresholds were always substantially higher in *Slc4a7*$^{-/-}$ mice than in *Slc4a7*$^{+/+}$ mice (**Fig. 5d**). A threshold difference of 20 dB was detected at 32 kHz, indicating a mild auditory impairment. Histologic analysis of the inner ear showed that mid and apical regions of the cochlea appeared normal in *Slc4a7*$^{-/-}$ mice (data not shown), but the basal region of the cochlea had histologic abnormalities. At one month of age (**Fig. 5f**,**j**), inner and outer hair cells were degenerating and there were morphologic changes in the stria vascularis and spiral ligament in *Slc4a7*$^{-/-}$ mice. In addition, there was collapse of Reissner's membrane, suggesting that NBC3 is essential for endolymph production. By three months of age, there was more severe degeneration and loss of both inner and outer hair cells in *Slc4a7*$^{-/-}$ mice (**Fig. 5h**,**l**). Cochlear immunohistochemical staining showed that NBC3 was expressed in the spiral ligament throughout the cochlea in *Slc4a7*$^{+/+}$ mice (**Fig. 5m**), but the cotransporter was not detected in *Slc4a7*$^{-/-}$ mice (**Fig. 5n**). NBC3 was detected in type I fibrocytes beneath the stria vascularis, type II fibrocytes beneath the spiral prominence and type V fibrocytes in the suprastrial region (**Fig. 5m**). These findings establish the presence of NBC3 in the inner ear and are consistent with an important role for spiral ligament fibrocyte sodium bicarbonate cotransport in maintenance of normal basal cochlear organ of Corti morphology and auditory function.

The finding that spiral ligament fibrocytes express the electroneutral sodium bicarbonate cotransporter NBC3 is intriguing, given that several lines of evidence suggest that these cells function in cochlear fluid ion homeostasis, which is essential for maintaining hair cell morphology and normal auditory function[22,23]. In addition to K^+ transport, spiral ligament fibrocytes have been postulated to have an important role in H^+/base transport because they express carbonic anhydrase[22]. Furthermore, it has been hypothesized that, analogous to the K^+ recycling pathway, there is a bicarbonate recycling pathway in which transport by spiral ligament cells is integral[24]. Impaired ion transport by strial ligament fibrocytes is thought to be involved in the death of hair cells that occurs in age-related cochlear degeneration[23] and in the mouse model of DFN3 non-syndromic deafness[25,26]. These findings complement our results, which show the specific requirement for normal spiral ligament fibrocyte sodium bicarbonate flux mediated by NBC3 in preventing hair cell degeneration and maintaining normal auditory function. *Slc4a7*$^{-/-}$ mice provide the first example of hair cell degeneration resulting from loss of function of an inner ear acid-disposal transporter.

An intriguing feature of *Slc4a7*$^{-/-}$ mice is the associated impairment of both auditory and retinal function. This work indicates that *Slc4a7*$^{-/-}$ mice are a new model of Usher syndrome, the most frequent cause of various degrees of auditory impairment accompanied by visual loss in humans [9,26]. Three clinical subtypes have been defined. Usher syndrome type 1, the most severe form, is characterized by severe to profound hearing loss, absence of vestibular function and prepubertal onset of retinitis pigmentosa. Usher syndrome type 2 is responsible for

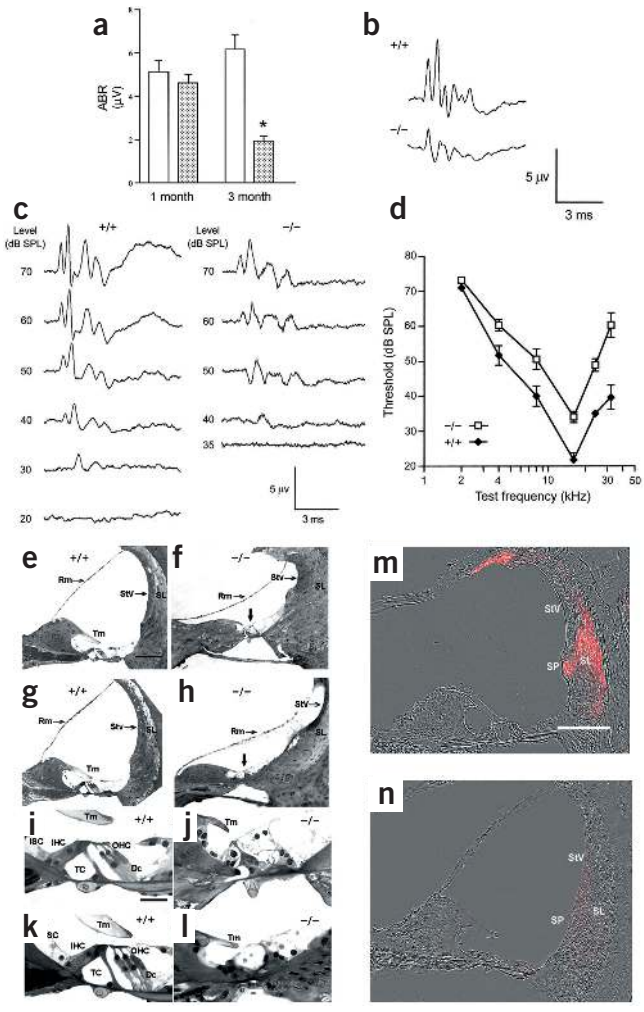

Figure 5 ABRs and histologic analysis of the cochlea in *Slc4a7*$^{-/-}$ mice. (**a**) Auditory impairment in *Slc4a7*$^{-/-}$ mice. ABR amplitudes in response to clicks for one- and three-month-old mice are shown according to genotype (*Slc4a7*$^{+/+}$, open bars; *Slc4a7*$^{-/-}$, filled bars). Amplitudes (in μV) were averaged across all stimulus intensities and ABR waves I, II and III (mean ± s.e.m., $n = 5$ in each group). *$P < 0.04$. (**b**) ABR waveforms induced by click stimuli (60 dB SPL) in three-month-old *Slc4a7*$^{+/+}$ (upper) and *Slc4a7*$^{-/-}$ (lower) mice. (**c**) 16-kHz tone burst evoked ABR waveforms in three-month-old *Slc4a7*$^{+/+}$ (left) and *Slc4a7*$^{-/-}$ (right) mice measured at various stimulus levels. (**d**) Mean ± s.e.m. ABR thresholds in *Slc4a7*$^{+/+}$ (closed diamonds) and *Slc4a7*$^{-/-}$ mice (open squares) in response to tone-burst stimuli (8–10 three-month-old mice tested per group, $P < 0.05$). (**e–l**) Morphological analysis of the cochlea in *Slc4a7*$^{-/-}$ mice. (**e–h**) Basal cochlea, low magnification. (**e**) *Slc4a7*$^{+/+}$, one month old, scale bar = 100 μm. (**f**) *Slc4a7*$^{-/-}$, one month old. (**g**) *Slc4a7*$^{+/+}$, three months old. (**h**) *Slc4a7*$^{-/-}$, three months old. (**i–l**) Higher magnification of the organ of Corti. (**i**) *Slc4a7*$^{+/+}$, one month old, scale bar = 30 μm. (**j**) *Slc4a7*$^{-/-}$, one month old. (**k**) *Slc4a7*$^{+/+}$, three months old. (**l**) *Slc4a7*$^{-/-}$, three months old. At one month of age (**f**,**j**), *Slc4a7*$^{-/-}$ cochlea showed morphologic changes that consist of collapse of Reissner's membrane (Rm), degenerating inner hair cells (IHC) and outer hair cells (OHC; arrow) and morphologic changes in the stria vascularis (StV) and spiral ligament (SL). At three months of age, there was evidence for more severe degeneration and loss of both inner and outer hair cells in *Slc4a7*$^{-/-}$ mice (**h**,**l**). In addition, by three months of age there was moderate loss of spiral ganglion neurons (data not shown). Dc, Deiter's cell; ISC, inner sulcus cell; TC, tunnel of Corti; Tm, tectorial membrane. (**m**) Confocal fluorescence images of the cochlea from three-month-old *Slc4a7*$^{+/+}$ mice. NBC3 is localized to spiral ligament fibrocytes. NBC3 was detected in type I fibrocytes beneath the stria vascularis, type II fibrocytes beneath the spiral prominence (SP) and type V fibrocytes in the suprastrial region. An identical pattern of expression was detected at ages 1–12 months. Scale bar = 200 μm. (**n**) Absence of NBC3 in the cochlea of *Slc4a7*$^{-/-}$ mice.

more than half of Usher syndrome cases and is characterized by mild to moderate auditory impairment, retinitis pigmentosa and normal vestibular function. Usher syndrome type 3 is a rare subtype, characterized by progressive hearing loss, retinitis pigmentosa and variable vestibular dysfunction. To date, mutations in seven distinct genes are known to cause Usher syndrome. *SLC4A7*, which is located on human chromosome 3p22 (ref. 8), is a candidate gene for Usher syndrome type 2B that has been mapped to this chromosomal region in a single consanguineous Tunisian family with mild to moderate hearing impairment and retinitis pigmentosa[27,28].

Our findings have identified an essential role for NBC3 in maintaining sensory cell integrity in two vertebrate sensory systems. The specific visual and auditory phenotype resulting from NBC3 deficiency is unexpected, considering that the cotransporter is also expressed in transporting epithelia, such as kidney and epididymis[29,30]. The lack of severe morphologic or physiological abnormalities in these tissues indicates that only in the visual and auditory sensory systems is the loss of the cotransporter function not compensated by other H^+ disposal mechanisms.

METHODS

Generation of NBC3 deficient mice. We derived the *Slc4a7* targeting vector from the Lambda KOS system (Lexicon Genetics). We generated the yeast selection cassette by PCR. This marker was introduced into the genomic clone by yeast recombination and resulted in the deletion of 148 bp of exon 5 (**Fig. 1a**). We electroporated the *Not*I-linearized vector into 129 Sv/Ev^{brd} (LEX1) embryonic stem (ES) cells. We isolated G418/FIAU resistant ES-cell clones and analyzed them for homologous recombination using Southern-blot analysis with a 384-bp 5′ PCR probe (**Fig. 1b**). Use of this probe on *Bam*H1-digested genomic DNA produced a wild-type band of 13 kb and a mutant band of 10.5 kb. Targeted ES-cell clones were injected into C57BL/6(albino) blastocysts and the resulting chimeras were mated to C57BL/6(albino) females. We genotyped tail DNA by PCR (**Fig. 1c**). We obtained null mutant mice (*Slc4a7*$^{-/-}$) and littermate controls (*Slc4a7*$^{+/+}$) in the expected mendelian ratio. All experiments were carried out in accordance with guidelines established by the institutional animal research committee of University of California Los Angeles.

Immunoblotting. We disrupted the eyes at 0 °C in 20 mM Tris-HCl, pH 7.5, containing 140 mM NaCl, 5% sucrose, 1 mM phenyl methyl sulfonylfluoride, 1 mM EDTA, 1 μg ml^{-1} pepstatin, 1 μg ml^{-1} leupeptin and 1 μg ml^{-1} aprotinin (all proteinase inhibitors were from Roche). The homogenate was centrifuged at 300*g* for 10 min and the supernatant was centrifuged at 4,000*g* for 10 min. We centrifuged the supernatant at 150,000*g* for 2 h and resolved the pellet on 10% ready gels from Bio-Rad in the presence of sodium dodecylsulfate. For immunoblotting, proteins were electrotransferred from the gel to PVDF membrane (Amersham Biosciences). The rabbit polyclonal antibody (dilution of 1:1,000) against the C terminus of human NBC3 has been extensively characterized in various species[29,30]. In control experiments, the primary antibody was preincubated with immunizing peptide (data not shown). Secondary horseradish peroxidase–conjugated mouse antibody to rabbit (Jackson Immunoresearch) was used at a dilution of 1:10,000. We visualized the bands using an ECL kit and ECL Hyperfilm from Amersham Biosciences.

Fundus exam. We examined the eyes with a slit lamp (Nikon) in conjunction with a 60– or 90–diopter (D) condensing lens. We dilated the pupils with a drop of 1% cyclopentolate and 1% atropine (Alcon Laboratory). We used a small animal fundus digital camera and imaging system (Kowa Genesis) to photograph mouse fundi. The instrument was used in conjunction with a 60D or 90D lens (Volk) mounted between the camera and eye. Photographs were taken using conscious mice to avoid complications of anesthesia such as clouding of the ocular media. We trimmed the vibrissae with fine scissors to prevent them from obscuring the photograph.

Retinal morphology and immunocytochemistry. We anesthetized the mice with 25 μl 2.5% Avertin (stock solution: 10 g tribromoethyl alcohol in 10 ml tertiary amyl alcohol diluted to 2.5% with phosphate-buffered saline) per g body weight. They were fixed by transcardiac perfusion with 1% formaldehyde and 2% glutaraldehyde buffered with 0.1 M sodium phosphate, pH 7.2. We then removed the eyes and bisected them along the vertical meridian into nasal and temporal hemispheres. One hemisphere from each eye (that contained the optic nerve head) was fixed additionally for 1 h with 1% osmium tetroxide (OsO_4) dissolved in 0.1 M sodium phosphate buffer, pH 7.2, then dehydrated and embedded in a 1:1 mixture of Epon 812 (Tousimis) and Araldite 502 (Electron Microscopy Sciences) epoxy resins. We cut sections of the entire retina, including the optic nerve head, at 0.5 mm and stained them with 1% toluidine blue. Sections were viewed and imaged in a Zeiss Axioplan microscope (Carl Zeiss) equipped with a CoolSNAP digital camera (Media Cybernetics) and Image Pro Plus software (Media Cybernetics). We bisected the second hemisphere from each eye into superior and inferior quadrants, fixed them in OsO_4 as described above, dehydrated them and embedded them in Araldite 502. We stained sections with a light gold interference color with uranium and lead salts and imaged in a Zeiss EM910 electron microscope (Carl Zeiss).

For immunofluorescence experiments, we removed mouse eyes and immediately froze them in dry ice. We applied the extensively characterized antibody to NBC3 (refs. 29,30; 1:100 dilution) to 5-μm cryostat sections for 45 min, washed sections several times in phosphate-buffered saline and then applied goat antibody to rabbit IgG conjugated with Alexa 594 (1:500 dilution; Molecular Probes) for 40 min. In control experiments, the primary antibody was preabsorbed with the specific immunizing peptide (data not shown). We washed the slides in phosphate-buffered saline and mounted them in Cytoseal 60 (Stephens Scientific). We captured the confocal images with a Leica TCS SP inverted confocal Microscope using a krypton laser (model 643, Melles Griot). We studied multiple sections from different mice.

Electroretinography. After 2 h of dark-adaptation, we anesthetized mice by intraperitoneal injection of 15 μg ketamine and 7 μg xylazine per g body weight in saline solution. We recorded ERGs from the corneal surface of one eye after pupil dilation (1% atropine sulfate) using a gold loop corneal electrode together with a mouth reference and tail ground electrode. Stimuli were produced with a Grass Photic Stimulator (PS33 Plus, Grass Instruments) affixed to the outside of a highly reflective Ganzfeld dome. Signals were amplified (× 10,000; 1–1,000 Hz; CP511 AC amplifier, Grass Instruments), digitized (PCI-1200, National Instruments) and computer-analyzed using custom software in a personal computer. We monitored body temperature with a rectal probe and maintained a constant temperature of 38 °C. We recorded rod-mediated responses to short-wavelength (λ_{max} = 449 nm) flashes of light flashes over a 3.0 log range of intensities (0.3 log unit steps) up to the maximum allowable by the photic stimulator (0.668 cd-s m^{-2}). To analyze the responses to blue light, we fitted the intensity versus amplitude response curves to the Naka-Rushton function, $V/V_{max} = I/(I + k)$, where V = rod peak-to-peak amplitude, V_{max} = maximum rod amplitude, I = retinal illuminance and k = retinal illuminance at half amplitude. The rod ERG threshold (2.0 μV criterion) was derived from the Naka-Rushton parameters, such that log threshold = $\log k + 0.3 - \log(V_{max} - 2)$.

Single-rod photocurrent responses. We placed freshly dissected retinas from mice, dark-adapted for approximately 3 h, in Locke's solution (140 mM NaCl, 3.6 mM KCl, 1.2 mM $CaCl_2$, 2.4 mM $MgCl_2$, 0.02 mM EDTA, 10 mM glucose, 5 mM ascorbic acid and 3 mM HEPES buffer, pH 7.4) and chopped them into small sections with a sharp razor blade. We pipetted the sections onto a coverslip on the stage of an inverted Zeiss microscope (Axiovert 135 TV). We perfused the sections at 2–4 ml min^{-1} with 25 mM bicarbonate buffered Dulbecco's modified Eagle's medium supplemented with 5 mM succinic acid, 0.5 mM glutamic acid and 5 mM gluconic acid (as Na^+ salts) and bubbled with 5% CO_2/95% O_2, pH 7.4, at 37 °C. All manipulations were done under dim red light or infrared illumination with a converter (FJW Optical Systems) for visualization. The preparation on the microscope was viewed remotely using a small television monitor attached to a CCD camera (Oscar, Mintron USA). We recorded suction pipette currents with a patch-clamp amplifier (Model PC501-A, Warner Instruments), low-pass filtered at 35 Hz (Bessel filter, Frequency Devices) and sampled at 100 Hz with a PC-compatible computer using

PCLAMP software (Axon Instruments). We analyzed the digitized currents using Origin software (Microcal). Light stimuli were delivered from a dual-beam optical bench using a 500 nm interference filter, stimulus intensity was controlled with absorptive neutral density filters and with a calibrated silicon photodiode (Graseb Optromics). For single-photon responses, multiple responses to a dim (~50 photons per μm^2 per s) 20-ms flash of 500-nm light were averaged, and the squared mean was compared to the time-dependent variance. The squared mean was multiplied by a factor so that its rising phase superimposed onto the variance. This factor, which represents the reciprocal of the average number of photoisomerizations of the rhodopsin chromophore, 11-cis retinal, per flash was then used to adjust the mean response to the single photon level.

Apoptotic nuclear staining. We fixed the eyes in 4% paraformaldehyde for 6 h and then immersed them overnight in 30% sucrose. We used the *in situ* cell death detection kit TMR red (Roche) to detect apopotic nuclei. Frozen 10-µm tissue sections were immersed in 10 µg ml^{-1} of proteinase K nuclease free buffer (Roche) with 10 mM Tris/HCL, pH 7.4, for 2 min at 4 °C. We rinsed the sections repeatedly with phosphate-buffered saline and then applied 50 µl of the TUNEL reaction mixture. We incubated the slides in a humidified chamber atmosphere for 60 min at 37 °C in the dark. At the end of the incubation, the slides were washed repeatedly with phosphate-buffered saline and incubated for a further 10 min. For control slides, we omitted the TUNEL reaction mixture from the labeling solution, and no staining was detected.

Auditory tests. We recorded ABR in mice anesthetized with Avertin. Stimuli consisted of acoustic clicks (100 µs duration, alternating polarity, 11.8 per s) delivered through an Etymotic ER3A tubephone and 3-mm rubber tube inserted into the meatus. Stimulus intensity (with 0 dB attenuation) was 69 dB sound-pressure level (SPL). Each mouse received an intensity series of 0, –10, –20, –25, –30, –25, –20, –10 and 0 dB attenuation. We recorded the electroencephalogram (EEG; Grass P511 amplifier, bandpass 30–3,000 Hz) from subcutaneous needle electrodes inserted at the scalp vertex, behind and below the ipsilateral ear, and forehead (ground electrode). The real-time computer data acquisition program automatically eliminated all EEG samples containing heart rate or other large amplitude artifacts. Each brainstem auditory evoked response average was based on 1,000 artifact-free samples. We determined hearing thresholds as a function of frequency with stimuli consisting of sine-wave tone bursts (1 ms rise/fall; 2 ms plateau) at 2, 4, 8, 16, 24 and 32 kHz. We downloaded waveforms to a Berkeley Nucleonics Model 630 arbitrary function generator. Output of the function generator was triggered by the averaging computer, adjusted by an external dB attenuator and fed to an Intelligent Hearing Systems high-frequency audio transducer. Monaural stimulation was delivered through a 10-cm length of polyethylene tubing into the ear canal. A second parallel tube connected to an Etymotic ER-10C otoacoustic microphone allowed verification of stable placement in the ear canal throughout the experiment (tested with a 2 kHz calibration tone between ABR runs). We obtained a standard response at 0 dB attenuation for each frequency to define wave components. We reduced sound levels systematically until ABR waves were no longer detected (threshold). We adjusted external dB settings for Intelligent Hearing Systems– calibrated differences in transducer output at each frequency.

Inner ear morphology and immunocytochemistry. We anesthetized and perfused mice as described above except that they were fixed with 4% paraformaldehyde buffered with 0.1 M sodium phosphate, pH 7.2. We removed the left and right temporal bones from the skull. We used the left temporal bone for immunohistochemical staining of the inner ear. The right temporal bone was used for morphological analysis and was postfixed in a solution containing 2% glutaraldehyde and 4% paraformaldehyde for 24 h. The tissue was then immersed in a 1% osmium tetroxide phosphate-buffered solution for 1 h, washed with phosphate buffer and placed in a decalcifing solution (3% EDTA in a buffered phosphate solution) for 7 d. The auditory bullae containing the cochlea were further microdisected, dehydrated and embedded in EPON-810. We cut sections of 3 µm using a Sorvall MT2 ultramicrotome. We counterstained the sections with 1% toluidine blue buffered solution, mounted them on coverslips and viewed and imaged them in a Nikon Eclipse E800 microscope. The left ears were postfixed in the same fixative for 6 h and decalcified by immersion in a 3% EDTA buffered phosphate solution for 3 d. The auditory bullae were further microdissected and immersed in 30% sucrose for 3 d. Before we sectioned the inner ear, we removed the tissue from the sucrose, immersed it in Tissue Tek (Polyscience) and placed it under vacuum for 3 h. The cochlea was properly oriented to obtain cross-sections of the organ of Corti (mid-modiolar sections). We obtained 14-µm thick serial sections using a Microm HM 500 cryostat (Zeiss). The sections were mounted on Superfrost plus slides and stored at –80 °C until used. For immunohistochemical staining, we applied the primary antibody to NBC3 (refs. 29,30; 1:100 dilution) to the tissue sections incubated in a humidified chamber at 4 °C for 48 h. In control experiments, the primary antibody was preabsorbed with the specific immunizing peptide (data not shown). After washing sections several times in phosphate-buffered saline, we applied goat antibody to rabbit IgG conjugated with Alexa 594 (1:500 dilution; Molecular Probes) for 40 min. We studied multiple sections from different mice.

URL. Detailed information regarding the genes causing Usher syndrome can be obtained used a public web-based server (RetNet) at http://www.sph.uth.tmc.edu.

ACKNOWLEDGMENTS

We thank D. Petrasek and S.H. Tsang for their helpful suggestions. This work was supported by grants from the US National Institutes of Health, the Foundation Fighting Blindness, the Factor Family Foundation and the National Kidney Foundation.

COMPETING INTERESTS STATEMENT

The authors declare that they have no competing financial interests.

Received 19 March; accepted 30 April 2003
Published online 15 June 2003; doi:10.1038/ng1176

1. Bianchi, L. & Driscoll, M. Protons at the gate: DEG/ENaC ion channels help us feel and remember. *Neuron* **34**, 337–340 (2002).
2. Waldmann, R. Proton-gated cation channels—neuronal acid sensors in the central and peripheral nervous system. *Adv. Exp. Med. Biol.* **502**, 293–304 (2001).
3. Gross, E. & Kurtz, I. Structural determinants and significance of regulation of electrogenic Na^+-HCO_3^- cotransporter stoichiometry. *Am. J. Physiol. Renal Physiol.* **283**, F876–F887 (2002).
4. Krulwich, T.A. Alkaliphiles: 'basic' molecular problems of pH tolerance and bioenergetics. *Mol. Microbiol.* **15**, 403–410 (1995).
5. Denison, S.H. pH regulation of gene expression in fungi. *Fungal Genet. Biol.* **29**, 61–71 (2000).
6. Csete, M.E. & Doyle, J.C. Reverse engineering of biological complexity. *Science* **295**, 1664–1669 (2002).
7. Pushkin, A. *et al.* Cloning, tissue distribution, genomic organization, and functional characterization of NBC3, a new member of the sodium bicarbonate cotransporter family. *J. Biol. Chem.* **274**, 16569–16575 (1999).
8. Pushkin, A. *et al.* Mapping of the human *NBC3* (*SLC4A7*) gene to chromosome 3p22. *Genomics* **58**, 321–322 (1999).
9. Kimberling, W.J., Orten, D. & Pieke-Dahl, S. Genetic heterogeneity of Usher syndrome. *Adv. Otorhinolaryngol.* **56**, 11–18 (2000).
10. Pittler, S.J. & Baehr, W. Identification of a nonsense mutation in the rod photoreceptor cGMP phosphodiesterase beta-subunit gene of the rd mouse. *Proc. Natl. Acad. Sci. USA* **88**, 8322–8326 (1991).
11. Travis, G.H., Groshan, K.R., Lloyd, M. & Bok, D. Complete rescue of photoreceptor dysplasia and degeneration in transgenic retinal degeneration slow (rds) mice. *Neuron* **9**, 113–119 (1992).
12. Hao, W. *et al.* Evidence for two apoptotic pathways in light-induced retinal degeneration. *Nat. Genet.* **32**, 254–260 (2002).
13. Krizaj, D. & Copenhagen, D.R. Calcium regulation in photoreceptors. *Front. Biosci.* **7**, 2023–2044 (2002).
14. Fain, G.L., Matthews, H.R., Cornwall, M.C. & Koutalos, Y. Adaptation in vertebrate photoreceptors. *Physiol. Rev.* **81**, 117–151 (2001).
15. Trapp, S., Luckermann, M., Kaila, K. & Ballanyi, K. Acidosis of hippocampal neurones mediated by a plasmalemmal Ca^{2+}/H^+ pump. *Neuroreport* **7**, 2000–2004 (1996).
16. Krizaj, D., Demarco, S.J., Johnson, J., Strehler, E.E. & Copenhagen, D.R. Cell-specific expression of plasma membrane calcium ATPase isoforms in retinal neurons. *J. Comp. Neurol.* **451**, 1–21 (2002).
17. Koulen, P., Fletcher, E.L., Craven, S.E., Bredt, D.S. & Wassle, H. Immunocytochemical localization of the postsynaptic density protein PSD-95 in the mammalian retina. *J. Neurosci.***18**, 10136–10149 (1998).
18. DeMarco, S.J. & Strehler, E.E. Plasma membrane Ca^{2+}-ATPase isoforms 2b and 4b interact promiscuously and selectively with members of the membrane-associated guanylate kinase family of PDZ (PSD95/Dlg/ZO-1) domain-containing proteins. *J. Biol. Chem.* **276**, 21594–21600 (2001).

19. Pushkin, A. *et al.* The COOH termini of NBC3 and the 56-kDa H^+-ATPase subunit are PDZ motifs involved in their interaction. *Am. J. Physiol. Cell Physiol.* **284**, C667–C673 (2003).
20. Barnes, S., Merchant, V. & Mahmud, F. Modulation of transmission gain by protons at the photoreceptor output synapse. *Proc. Natl. Acad. Sci. USA* **90**, 10081–10085 (1993).
21. DeVries, S.H. Exocytosed protons feedback to suppress the Ca^{2+} current in mammalian cone photoreceptors. *Neuron* **32**, 1107–1117 (2001).
22. Spicer, S.S. & Schulte, B.A. Differentiation of inner ear fibrocytes according to their ion transport related activity. *Hear. Res.* **56**, 53–64 (1991).
23. Spicer, S.S., Gratton, M.A. & Schulte, B.A. Expression patterns of ion transport enzymes in spiral ligament fibrocytes change in relation to strial atrophy in the aged gerbil cochlea. *Hear. Res.* **111**, 93–102 (1997).
24. Salt, A.N. Dynamics of the Inner Ear Fluids. in *Physiology of the Ear* 333–356 (Singular/Thompson Learning, San Diego, 2001).
25. Minowa, O. *et al.* Altered cochlear fibrocytes in a mouse model of DFN3 nonsyndromic deafness. *Science* **285**, 1408–1411 (1999).
26. Steel, K.P. & Kros, C.J. A genetic approach to understanding auditory function. *Nat. Genet.* **27**, 143–149 (2001).
27. Hmani, M. *et al.* A novel locus for Usher syndrome type II, USH2B, maps to chromosome 3 at p23–24.2. *Eur. J. Hum. Genet.* **7**, 363–367 (1999).
28. Hmani-Aifa, M. *et al.* Distinctive audiometric features between USH2A and USH2B subtypes of Usher syndrome. *J. Med. Genet.* **39**, 281–283 (2002).
29. Pushkin, A. *et al.* NBC3 expression in rabbit collecting duct: colocalization with vacuolar H^+-ATPase. *Am. J. Physiol.* **277**, F974–F981 (1999).
30. Pushkin, A., Clark, I., Kwon, T.H., Nielsen, S. & Kurtz, I. Immunolocalization of NBC3 and NHE3 in the rat epididymis: colocalization of NBC3 and the vacuolar H^+-ATPase. *J. Androl.* **21**, 708–720 (2000).